fluids

MDPI

Article

Effects of Head Posture on Inhaled Particle Deposition and Upper-Airway Penetration

Xinying Liu, Brenda Vara Almirall and Kiao Inthavong*

Department of Mechanical Manufacturing Mechatronic Engineering, RMIT University, Melbourne, VIC 3000, Australia; xinying.liu@rmit.edu.au (X.L.); brenda.almirall@rmit.edu.au (B.V.A.)
* Correspondence: kiao.inthavong@rmit.edu.au

Abstract

Targeted drug delivery in the respiratory tract must overcome inertial impaction at the oropharyngeal bend which typically captures the majority of inhaled particles before they reach the larynx or lungs. We investigated whether head posture can be used to control that impaction by altering upper-airway curvature. Four head postures of a simplified airway (flexion at 30°, neutral (0°), and extension at 30° and 60°) were simulated at inhalation flow rates of 10 L min^{-1} (laminar) and 30 L min^{-1} (k–ω SST turbulence), with particle trajectories tracked across aerodynamic diameters from 3 µm to 29 µm. The Dean number at the bend decreased from 1608 in flexion to 835 at 60° extension at 30 L min^{-1}. Regional particle deposition followed bend curvature rather than the head tilt angle. As the bend opened with extension, preferential deposition sites shifted 50 mm downstream toward the glottis. Total airway deposition varied with posture, peaking at 30° extension and reducing at 60° extension, where over 40% of coarse particles exited through the tracheal outlet. The posture-specific maximum in laryngeal deposition, each attained at its own optimal particle size, was highest at 30° extension and 30 L min^{-1} (26% at 9 µm), compared with 16% at 11 µm for the neutral posture and 11% at 13 µm in flexion. Head extension could therefore roughly double laryngeal drug delivery relative to neutral posture when paired with appropriate particle sizes, while extreme extension straightens the airway and allows a larger fraction of the inhaled dose to penetrate beyond the upper airway toward the lungs.

Keywords: laryngeal drug delivery; head posture;particle deposition; computational fluid dynamics; discrete phase model; Dean number

Check for updates

Academic Editor: D. Andrew S. Rees

Received: 24 September 2026
Revised: 19 October 2026
Accepted: 26 October 2026
Published: 2 November 2026

Copyright: © 2026 by the authors. Licensee MDPI, Basel, Switzerland. This article is an open access article distributed under the terms and conditions of the Creative Commons Attribution (CC BY) license.

1. Introduction

Targeted drug delivery with particles depends on where the particles deposit. When inhaled, particles move through the airways, guided by airflow during inhalation, and deposites in one of several anatomical zones along the respiratory tract [1,2]. For micron particles that are influenced by inertial properties, we can broadly categorise these into three zones that compete for the inhaled dose. Deep-lung delivery, required for asthma, chronic obstructive pulmonary disease (COPD), and cystic fibrosis, requires fine particle fractions that can reach the deep lungs [3]. Laryngeal delivery for local treatment of chronic laryngitis, vocal fold nodules, and subglottic stenosis [4], requires the opposite, with deposition within a narrow target positioned midway along the extrathoracic airway [5]. Positioned directly above the larynx is the oropharynx, which acts as a filter through which

any particle not already deposited must first pass. This is also where un-targeted deposition of inhaled corticosteroids can produce local dysphonia, and mucosal irritation [6–8].

This inertial behaviour of micron particle trajectories is governed by the Stokes number,

$$\mathrm{Stk} = \frac{\rho_p d_p^2 U}{18 \mu D} \tag{1}$$

where ρ_p is particle density, d_p is particle aerodynamic diameter, U is mean fluid velocity, μ is fluid dynamic viscosity, and D is a characteristic length such as the local airway diameter. Stk compares two timescales: the time a particle takes to relax to a change in the surrounding flow, against the time available for that flow to redirect it around a bend. Particles with $\mathrm{Stk} \ll 0.1$ relax fast enough to track the flow field essentially unperturbed; particles typically with $\mathrm{Stk} \gtrsim 0.1$ cannot, and are carried across streamlines toward the outer wall of any turn, where they impact [9]. This parameter is used in vitro deposition measurements in human airway casts that have correlated against the impaction parameter $d_p^2 Q$, where Q is volumetric flow rate, a direct empirical proxy for Stk at fixed geometry [10–14]. Because many therapeutic particles possess aerodynamic diameters between 1 and 20 µm [15,16], a substantial fraction of any inhaled dose sits inside this inertial regime.

The human extrathoracic airway consists of a succession of sharp directional changes. Air enters the oral cavity, turns downwards through the oropharynx, converges into the larynx, and turns again into the trachea toward the lung [17,18]. In curved conduits, fluid in the high-velocity core experiences centrifugal acceleration toward the outer radius, establishing adverse cross-stream pressure gradients that drive a pair of counter-rotating secondary vortices (Dean vortices) in the cross-section [19–21]. The intensity of this secondary motion is quantified by the Dean number,

$$\mathrm{De} = \mathrm{Re}\sqrt{\frac{D}{2R_c}} \tag{2}$$

where Re is the Reynolds number and R_c is the radius of curvature of the bend. A sharper turn (smaller R_c) yields a larger Dean number, more intense secondary vortices, and higher inertial impaction along the outer wall. Conversely, a gentler bend (larger R_c) weakens secondary motion and more particles are able to pass further downstream. Because R_c enters this expression directly, it is, in principle, an externally controllable parameter and any mechanism that changes the extrathoracic airway without altering flow rate or airway cross-section acts on deposition exclusively through this single geometric term.

We propose that head posture provides such a mechanism. The larynx and cervical trachea are held in place by surrounding tissue, cartilage, and muscle, but head tilt still noticeably changes the curve of the oral cavity and pharynx above them [22,23]. Neck flexion bends the head forward, closing the pharyngeal arch and sharpening the curve leading into the larynx while neck extension tilts the head backward, opening the arch and straightening the extrathoracic airway (Figure 1). Dynamic magnetic resonance imaging (MRI) studies in vocalists have shown that head-and-neck posture produces pronounced, measurable structural changes in vocal tract morphology [24], and posture is well known to influence global respiratory function more broadly [25,26]. Because head tilt directly modifies the bend radius R_c, it modulates the local Dean number and can shift the primary impaction site. Head posture is therefore, from a fluid mechanics standpoint, a zero-cost, patient-actuated boundary condition and adjusting it may enhance targeted deposition within the larynx for local disease management, avoid the oropharyngeal mucosa to

mitigate corticosteroid side effects, or straighten the airway to promote penetration past the extrathoracic airway for asthma or COPD management.

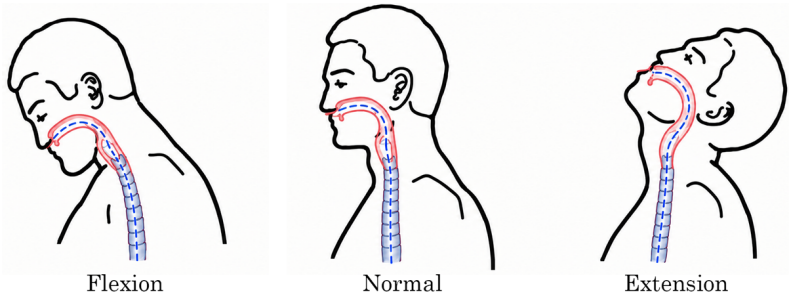


Figure 1. Schematic demonstrating the change in the upper-airway curvature associated with different head positions of flexion, normal, and extension positions.

Computational fluid dynamics (CFD) combined with Lagrangian discrete phase modelling provides an ideal framework to isolate this mechanism, resolving velocity fields and individual particle trajectories throughout airway anatomies [1,3,27]. While prior CFD studies have shown that inter-subject variations in mouth–throat morphology significantly alter particle deposition [28–30], these investigations only looked at a single, neutral head position (about 0°).

Studies related to head position originate primarily from anaesthesiology, where tilting the head back into the "sniffing position" helps line up the oral, pharyngeal, and laryngeal axes for tracheal intubation [31–33], but these studies focus on keeping the airway open during medical procedures rather than particle transport. More recently, Vara Almirall et al. [34] evaluated the impact of oral airway geometries on extrathoracic deposition, by comparing open-mouth oral inhalation airway geometry against the closed-mouth nasal breathing geometry commonly captured during supine imaging scans. However, how systematic changes in head tilt, isolated as a purely geometric change of a simplified airway, redistribute particle deposition between the oropharynx, larynx, and lower airway has not been established.

In this study, we treat head tilt as a controlled geometric variable and investigate whether it can be used to change particle deposition and penetration by systematically varying the curvature of the oropharyngeal bend. Four postures were constructed from a single simplified airway model, by rotating the oral cavity and pharynx about a fixed laryngeal axis through prescribed angles of: flexion at 30°, neutral (0°), and extension at 30° and 60°, and keeping the laryngeal and tracheal geometry constant. This made the curvature of the oropharyngeal bend the principal independent variable; the modest changes in supraglottic cross-sectional area and path length that necessarily accompany the re-blending of the rotated passage are quantified in Section 2.2 and their possible influence is considered in Section 4. These four geometries were evaluated under steady inhalation flow rates of 10 and 30 L min^{-1}. By combining airflow dynamics with Lagrangian tracking for particle diameters spanning 3 µm to 29 µm, we identified the physical mechanisms that either maximise laryngeal delivery or promote penetration beyond the modelled upper airway, using parameters such as the bend radius and Dean number. The neutral-posture results were also benchmarked against published oral-airway deposition correlations expressed in terms of the impaction parameter, so that, with particle size and flow rate accounted for, the differences between postures can be attributed to the change in airway curvature.

2. Method

2.1. Airway Geometry and Head Postures

A simplified extrathoracic airway geometry was adapted from the anatomical model of Cheng et al. [35], Zhang and Kleinstreuer [36], which has been widely employed and benchmarked in particle deposition investigations [2,37–39]. Figure 2 shows the four head postures in the mid-sagittal plane.

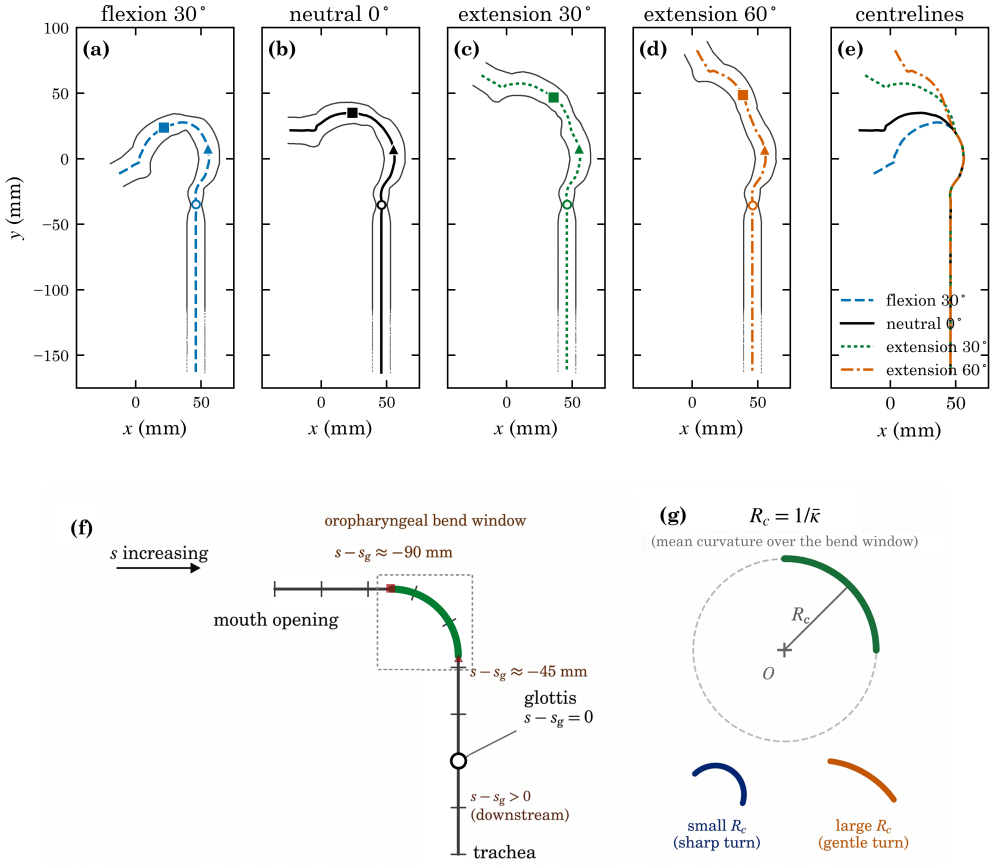


Figure 2. The four head postures in the mid-sagittal plane. (**a**–**d**) airway wall outline with a centreline overlaid; the open circle marks the glottis and is the minimum cross-sectional area. (**e**) the four centrelines superimposed, showing that the larynx and trachea are common to all four models. The triangle markers represent $s_{\mathrm{rel}} = s - s_{\mathrm{g}} \approx -45$ mm and the square markers represent $s_{\mathrm{rel}} \approx -90$ mm locations from the glottis. (**f**) s_{rel} arc length is measured relative to the glottis, where $s_{\mathrm{rel}} = 0$. It is negative upstream in the oropharynx and positive downstream in the trachea. The oropharyngeal bend window, approximately $-90 \leq s_{\mathrm{rel}} \leq -45$ mm is highlighted. (**g**) R_c is the reciprocal of the mean centreline curvature $\bar{\kappa}$.

The neutral configuration (0°) represents the airway in its baseline anatomical alignment which is in its original position from Zhang and Kleinstreuer [36]. Tilted configurations were constructed by pivoting the oral cavity and pharynx about the laryngeal axis while maintaining a fixed tracheal orientation. A tangential circular arc was used to smoothly blend the repositioned oral passage into the stationary laryngeal inlet, ensuring continuity of the airway cross-section. Three tilted models were generated: 30° flexion (chin toward chest), 30° extension (chin tilted backward), and 60° extension (pronounced backward tilt). The laryngeal airway and the trachea were kept identical across all four models to isolate posture-induced changes in the supraglottic airway. Because the blending arc must be tangent to both the rotated oral passage and the fixed laryngeal inlet, its radius and length are dictated by the angular and positional mismatch between the two tangents for each rotation angle rather than prescribed independently. For flexion and 60° extension

the rotated oral exit fell close enough to the laryngeal inlet that the arc length matched the neutral model to within 1 mm, whereas for 30° extension the tangency condition required a longer connecting arc, lengthening the mouth-to-larynx centreline by 9.1 mm (Table 1). This additional length lies entirely upstream of the larynx; since all axial positions are referenced to the glottis, it appears as an upstream displacement of the mouth opening in Figure 3, and its possible contribution to the deposition results is discussed in Section 4. To ensure realistic, unconstrained inhalation conditions, a hemispherical external dome was constructed around the mouth opening (Figure 4). This ambient domain allowed air and inhaled particles to enter the oral cavity naturally through pressure-driven entrainment, avoiding artificial velocity profiles or uniform face boundaries at the lips.

Table 1. Geometric characterisation measured from the meshes. All quantities are measured along the airway centreline, from the mouth opening (m) to the tracheal outlet. R_c is the radius of curvature of the mean oropharyngeal centreline. $\Delta s_{m\to l}$ is the centreline arc length from the mouth opening to the laryngeal inlet (l, about 11 mm upstream of the glottis) and $\Delta\theta_{m\to l}$ the net rotation of the centreline tangent over that length; $\Delta\theta_{\mathrm{tot}}$ is the net rotation from the mouth opening to the tracheal outlet, and L the total centreline length. Angles are signed so that the mouth-to-trachea turn is positive. The glottis area is $A_g = 0.567$ (cm^2) and the tracheal diameter is ≈ 13.56 mm.

Posture	R_c (mm)	$\Delta s_{m\to l}$ (mm)	$\Delta\theta_{m\to l}$ (deg)	$\Delta\theta_{\mathrm{tot}}$ (deg)	L (mm)
Flexion 30°	23.6	131.1	133.0	118.7	270.2
Neutral 0°	33.5	131.1	101.9	88.4	270.1
Extension 30°	49.9	140.2	72.7	58.2	279.2
Extension 60°	84.3	131.1	40.8	28.3	269.1

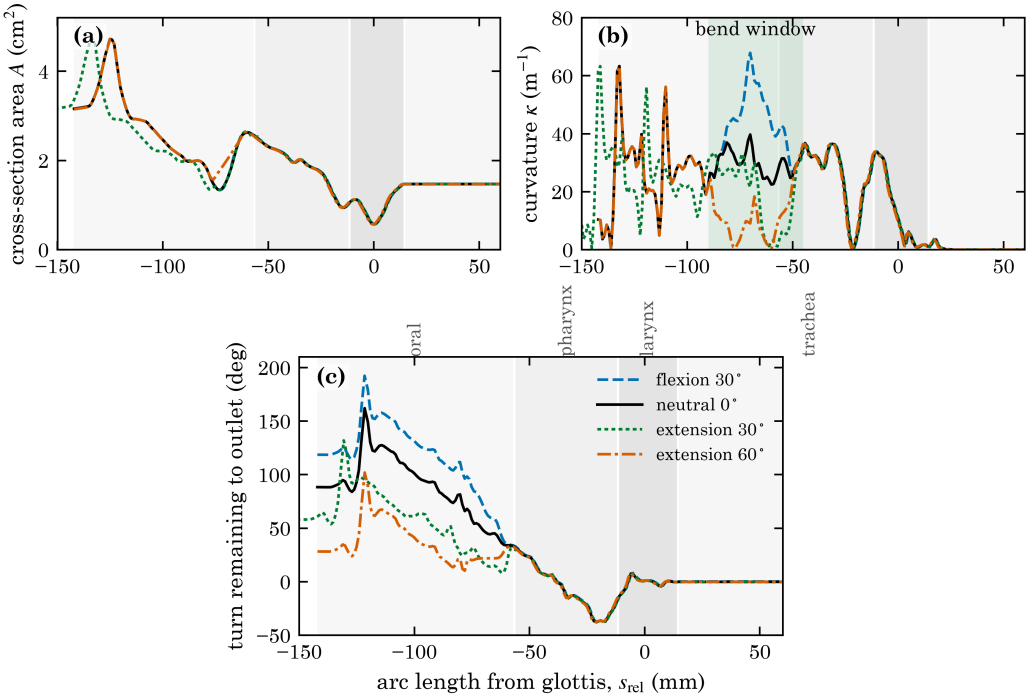


Figure 3. Centreline properties against arc length referenced to the glottis, s_{rel}. (**a**) airway cross-sectional area; (**b**) curvature, with the oropharyngeal bend window $-90 \le s_{\mathrm{rel}} \le -45$ mm shaded; (**c**) the turn still to come before the tracheal axis is reached. Downstream of $s_{\mathrm{rel}} = -45$ mm the four postures are geometrically indistinguishable; upstream they differ by up to 41% in area and 58 m^{-1} in curvature.

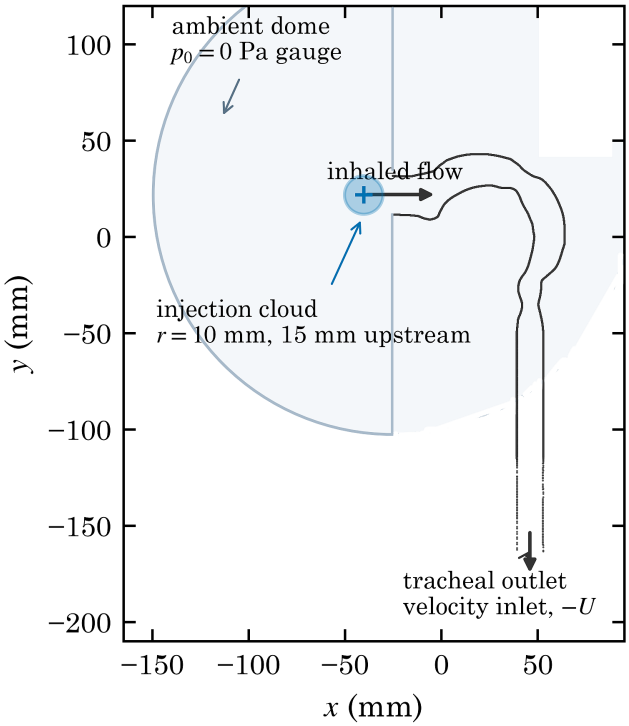


Figure 4. Computational domain and boundary conditions, neutral posture. The airway opens into a hemispherical ambient reservoir held at zero gauge total pressure, so inhaled air and particles enter the mouth without an imposed inlet profile. Flow is driven by a negative velocity inlet at the tracheal outlet. The shaded sphere is the particle injection cloud, 10 mm in radius and centred 15 mm in front of the mouth rim.

2.2. Geometric Characterisation

Airway geometry was quantified by slicing the airway surface walls with a sequence of cross-sectional planes oriented normal to the local centreline at 1 mm axial intervals. This procedure extracted the airway centreline coordinates, local cross-sectional area, perimeter, and curvature. Two anatomical landmarks served as reference locations across all cases. The glottis was defined as the point (s_g) where the airway cross-sectional area is smallest. Because the larynx was held rigid when building the CAD model, this narrowest point is the same across all four geometries, so it was used as a fixed reference point. Position along the airway centreline was measured relative to the glottis and denoted $s_{\mathrm{rel}} = s - s_{\mathrm{g}}$ so that $s_{\mathrm{rel}} = 0$ at the glottis and negative values lie upstream toward the mouth; this lets curvature, area, velocity, and deposition results from different postures be plotted on one shared axis. Comparisons between postures at a given s_{rel} are therefore comparisons at equal centreline distance from the glottis rather than between anatomically corresponding sections; because the oral cavity is rigidly rotated and the blending arc is re-generated for each posture, a given value of s_{rel} upstream of the bend can fall on different anatomical structures in different postures. The oropharyngeal bend over a fixed section is approximately, $s_{\mathrm{rel}} = -90$ to -45 mm. The centreline curvature was averaged to give $\bar{\kappa}$, and its reciprocal defines the bend radius $R_c = 1/\bar{\kappa}$, which describes how tight or gentle the throat bend is, where a small R_c means a sharp turn and a large R_c means a gentle, almost straight passage. Table 1 lists the key geometric values.

2.3. Meshing

Computational grids were generated using Ansys Fluent Meshing with surface-conforming polyhedral cells with six boundary prism layers resolving near-wall velocity gradients, and octree-based hexahedral cells filling the core flow domain (Figure 5). Cell

counts across the four meshes ranged from 1.193×10^6 to 1.244×10^6 cells (Table 2), with identical global, body-of-influence and near-wall sizing applied to every posture so that the four meshes differ only through the geometry they discretise. The sizing was selected with the mesh-independence protocol of Inthavong et al. [40], developed for the nasal cavity, which provides the initial size settings and the plane-subtraction technique, in which the velocity fields of successively refined meshes are mapped onto a common mid-sagittal plane and subtracted; the differences were quantified with the normalised error measures of Frank-Ito et al. [41]. Applied to the 30° flexion airway at 30 L min^{-1}, which has the sharpest bend of the four postures, with meshes of 0.31×10^6 to 5.52×10^6 cells, the normalised mean square error of the mid-sagittal velocity relative to the finest mesh fell from 0.32 for the coarsest mesh to 0.07 for a 1.21×10^6-cell mesh, whose 0.4 mm body-of-influence sizing was adopted for all four postures. The study is reported in the Supplementary Material (Figure S1).

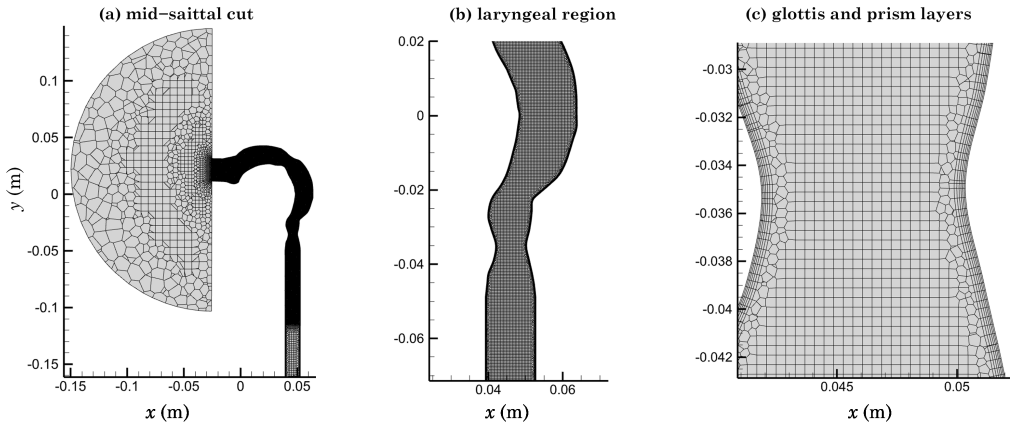


Figure 5. Mid-sagittal cut through the poly-hexcore volume mesh of the neutral posture, as used by the solver. Coordinates are in metres. (**a**) whole airway; (**b**) laryngeal region; (**c**) glottis, showing the near-wall prism layers. Boxes mark the region enlarged in the following panel.

2.4. Flow Modelling

Two steady inhalation flow rates were evaluated: 10 L min^{-1}, representing weak inhalation, representative of subjects with respiratory difficulty, and 30 L min^{-1}, representing deeper and faster inhalation of healthy lung function. The corresponding Reynolds numbers evaluated at the tracheal exit were 1069 and 3207, respectively (Table 2), based on the measured tracheal equivalent hydraulic diameter of 13.56 mm. The flow was modelled as steady and incompressible, governed by the Navier–Stokes equations:

$$\frac{\partial}{\partial x_i}(\rho u_i) = 0 \tag{3}$$

$$u_j \frac{\partial u_i}{\partial x_j} = -\frac{1}{\rho}\frac{\partial p}{\partial x_i} + \frac{\partial}{\partial x_j}\left((\nu + \nu_T)\frac{\partial u_i}{\partial x_j}\right) \tag{4}$$

where u_i is the time-averaged velocity component in direction x_i, p is static pressure, ρ is air density (1.225 kg m^{-3}), μ is dynamic viscosity (1.7894×10^{-5} Pa s), and $\nu = \mu/\rho$ and ν_T are kinematic and turbulent eddy viscosities, respectively. The inhaled air was treated as a single-phase fluid with constant density and viscosity; heat and water-vapour transfer between the airway mucosa and the inhaled stream, and the presence of gaseous pollutants, were not modelled. For the micron-sized inert particles considered here, these factors act on deposition only through their small influence on the air viscosity and density that enter the Stokes number (Equation (1)), and on hygroscopic particle growth, which is discussed in Section 5.

Table 2. Simulation matrix. Cell counts are for the shared mesh of each posture; both flow rates use the same mesh. Re_{tr} is evaluated at the tracheal outlet, and Re_b and De at the oropharyngeal bend (Section 2.2). Trajectories are per case, summed over the fourteen particle sizes.

Posture	N_{cells} ($\times 10^6$)	Q (L/min)	Turbulence Model	Re_{tr}	Re_b	De	Trajectories
Flexion 30°	1.214	10	Laminar	1069	920	536	280,000
Neutral 0°	1.197	10	Laminar	1070	919	449	280,000
Extension 30°	1.244	10	Laminar	1069	940	374	280,000
Extension 60°	1.193	10	Laminar	1071	891	278	280,000
Flexion 30°	1.214	30	k–ω SST	3207	2761	1608	560,000
Neutral 0°	1.197	30	k–ω SST	3210	2758	1347	560,000
Extension 30°	1.244	30	k–ω SST	3206	2819	1121	560,000
Extension 60°	1.193	30	k–ω SST	3214	2672	835	560,000

At 10 L min^{-1}, flow remained in the laminar regime ($\nu_T = 0$). At 30 L min^{-1}, turbulence was modelled using the shear-stress transport (SST) k–ω model, which blends the k–ω formulation in the viscous sublayer with the k–ϵ model in the outer wake region [42]. Airflow was driven by negative suction applied at the tracheal outlet, prescribed as a negative velocity-inlet magnitude normal to the boundary based on the measured outlet area, while the outer surface of the ambient dome was maintained at zero gauge total pressure (ambient atmosphere; Figure 4). At 30 L min^{-1}, inlet turbulence intensity was set to 1% with a turbulent viscosity ratio of 3.0 at both flow boundaries. Gravitational acceleration was specified as 9.81 m s^{-2} along the global $-y$ direction; because the trachea remained fixed in the vertical orientation, $-y$ aligned downward with anatomical gravity in all postures.

2.5. Discrete Phase Modelling

Particle transport was simulated using the Lagrangian discrete phase model (DPM) in Ansys Fluent. Because the volume fraction of the inhaled particle was dilute (<10^{-6}), one-way momentum coupling was employed, where the fluid field dictated particle trajectories without influence from particles to the continuous phase. Trajectories were calculated by integrating the force balance acting on individual spherical particles:

$$\frac{du_i^p}{dt} = f_D\left(u_i^f - u_i^p\right) + g_i \tag{5}$$

where superscripts f and p designate fluid and particle phases, g_i is gravitational acceleration, and f_D is the drag force per unit particle mass:

$$f_D = \frac{18\mu}{\rho_p d_p^2}\frac{C_d \mathrm{Re}_p}{24} = \frac{1}{\tau_p} \tag{6}$$

The particle Reynolds number is $\mathrm{Re}_p = \rho|u_i^f - u_i^p|d_p/\mu$, C_d is the spherical drag coefficient, and τ_p is the particle momentum relaxation time:

$$\tau_p = \frac{d_p^2 \rho_p}{18\mu}\frac{24}{C_d \mathrm{Re}_p} \tag{7}$$

The spherical drag law was adopted without Cunningham slip correction, as the slip correction over the diameter d range of 3 µm to 29 µm is below 6% at 3 µm and falls below 1% above 19 µm.

Fourteen monodisperse particle sizes were investigated: $d_p \in \{3, 5, 7, \ldots, 29\}$ µm, with a unit particle density of $\rho_p = 1000\,\mathrm{kg\,m^{-3}}$. Particles were released from rest ($u_i^p = 0$) within a spherical cloud of radius 10 mm positioned 15 mm upstream of the oral aperture along the mouth-rim normal (Figure 4). Particle coordinates within the cloud were distributed with a Halton sequence to produce a uniform spatial seeding for radial distributions. At $10\,\mathrm{L\,min^{-1}}$, 20,000 trajectories were tracked per size (280,000 trajectories per case). At $30\,\mathrm{L\,min^{-1}}$, turbulent dispersion was included via the Discrete Random Walk (DRW) model with four stochastic tries per particle, yielding 40,000 trajectories per size (560,000 trajectories per case). All airway walls, as well as the external face wall, were set to a 'trap' boundary condition upon contact; particles striking the face were recorded independently to ensure that reported deposition fractions reflect the true inhaled dose entering the oral cavity.

2.6. Numerical Procedure and Solution State

All airflow and particle simulations were performed with the finite-volume solver Ansys Fluent 2026 R1 (Ansys Inc., Canonsburg, PA, USA), with meshing in Ansys Fluent Meshing, geometric characterisation and deposition post-processing in Python 3.12 (NumPy, SciPy and Matplotlib), and flow visualisation in Tecplot 360. Simulations were run across 56 cores on the NCI Gadi supercomputing cluster. Pressure–velocity coupling used the Coupled scheme, while the spatial discretisation used second-order upwind schemes for momentum, turbulent kinetic energy, and specific dissipation rate, with least-squares cell-based gradient evaluations. Conservation of mass between the ambient dome and tracheal outlet closed to within 0.1% across all cases, and the peak-to-peak oscillation of the outlet throughput over the final 500 iterations was below 1.6%. For the particle tracking, zero particles deposited on the external dome or escaped through the ambient boundary, confirming that 100% of released particles entered the mouth. Furthermore, 99.975% of all released trajectories terminated in a definitive physical fate (wall trapping or tracheal escape), with only 0.025% as incomplete (i.e., reaching the 50,000-step tracking limit while airborne).

Deposition efficiencies are reported as the fraction of the released trajectories trapped in each region and are therefore deterministic for a given flow field at $10\,\mathrm{L\,min^{-1}}$. At $30\,\mathrm{L\,min^{-1}}$, where turbulent dispersion was represented stochastically, the four discrete-random-walk tries per injection point provide a measure of statistical uncertainty: with 40,000 trajectories per size, the standard error of a binomial deposition fraction η is $\sqrt{\eta(1-\eta)/N}$, which is at most 0.25% (absolute) at $\eta = 0.5$ and smaller elsewhere. Differences between postures reported below (typically 5–20 percentage points) therefore exceed the sampling uncertainty by more than an order of magnitude, and no further inferential statistics are applied to the simulation output.

3. Results

Figure 3 plots centreline airway properties as functions of arc length relative to the glottis (s_{rel}). Cross-sectional area (Figure 3a) was within9.4% across all four postures downstream of $s_{\mathrm{rel}} = -45$ mm, while upstream of the bend ($s_{\mathrm{rel}} < -45$ mm), by contrast, airway area varied by up to 41%. This upstream variation is a comparison at equal distance from the glottis (Section 2.2) and has two sources: the rigidly rotated oral cavity, whose cross-sections are unchanged in shape but are displaced along s_{rel} (and, for 30° extension, shifted upstream by the 9 mm longer blending arc), and the blended oropharyngeal segment itself, whose cross-section is re-generated for each posture. The largest local differences occur where the broad oral cavity of one posture is being compared with the narrower

oropharynx of another at the same s_{rel}, rather than from a change in the dimensions of any one anatomical section.

The curvature follows the same pattern (Figure 3b) where local curvatures were similar downstream of $s_{rel} = -45$ mm but varied significantly upstream, within the shaded oropharyngeal bend window ($-90 \leq s_{rel} \leq -45$ mm), as the different head postures represent a parametric variation of the oropharyngeal bend. In Table 1, this variation is captured by the oropharyngeal bend radius R_c, which increased with extension from 23.6 mm in flexion, to 33.5 mm at neutral, 49.9 mm at 30° extension, and 84.3 mm at 60° extension.

The "turn remaining to outlet" refers to how much more bending is left ahead of a position, before the path straightens out and lines up with the trachea axis (Figure 3c). This metric provides insight into how much directional change in the flow path still lies ahead of a particle at any given position, influencing deposition regions due to a particle Stokes number, and also identifies where along the airway the four head postures diverge geometrically and where they converge so any differences in deposition or secondary flow can be attributed specifically to the upstream head tilt bend rather than to changes near the outlet. From the oral opening to the trachea, the angular deflection was 118.7°, 88.4°, 58.2°, and 28.3° for 30° flexion, neutral (0°), 30° extension, and 60° extension, respectively. Correspondingly, the turn from the mouth opening to the laryngeal inlet dropped from 133.0° in flexion to 40.8° at 60° extension (Table 1).

3.1. Airflow Dynamics and Secondary Flow

Velocity magnitude contours and its profile along the airway centreline are presented in Figures 6 and 7. Across all postures, flow acceleration through the converging glottal constriction produced a characteristic laryngeal jet. Peak velocities reached $\approx$3.4m s^{-1} at 10 L min^{-1} and $\approx$9.8m s^{-1} at 30 L min^{-1}. Because the larynx and trachea region were invariant, the glottal jet structure collapsed onto the same profile downstream of $s_{rel} = -45$ mm (Figure 7).

Upstream flow patterns in the oropharynx, however, exhibited head posture dependence. In flexion, the air stream experienced a sharp 133° turn with a small bend radius ($R_c = 23.6$ mm), causing strong flow separation along the inner wall and displacing a high-velocity core toward the posterior pharyngeal wall. With increasing neck extension, the oropharyngeal curve straightened, weakening flow separation and aligning the velocity core with the airway centreline. Consequently, the Dean number at the bend decreased with extension (Table 2): from 536 in flexion to 278 at 60° extension at 10 L min^{-1}, and from 1608 to 835 at 30 L min^{-1}. Because the bend Reynolds number was nearly constant across postures (891 to 940 at 10 L min^{-1} and 2672 to 2819 at 30 L min^{-1}), variations in Dean number were primarily caused by changes in the bend radius R_c.

3.2. Total and Regional Particle Deposition

Regional deposition efficiencies as functions of aerodynamic diameter are plotted in Figure 8. Deposition in the oral cavity was negligible (<0.5%) across all particle sizes and flow rates. Inhaled particles entered through the mouth opening passively which allowed the particles to move through the oral cavity without hitting the walls, and deposition only occurred upon reaching the pharynx and larynx.

Total airway deposition varied with head posture. At 10 L min^{-1} and $d_p = 29$ µm, total deposition was 75.3% in flexion, 85.2% in neutral, 92.5% at 30° extension, but dropped to 51.6% at 60° extension. At 30 L min^{-1}, corresponding total deposition was 94.9%, 96.9%, 98.1%, and this dropped to 58.1% at 60° extension. Total deposition increased steadily from flexion through 30° extension before falling at 60° extension. The reduction in deposition found for the 60° extension model enabled substantial particle penetration past the tracheal

outlet of the model. While the other three postures captured over 95% of particles larger than 15 µm at 30 L min^{-1}, the 60° extension captured only 40% to 58%. Straightening the oropharyngeal curvature (R_c = 84.3 mm) significantly decreased inertial impaction, permitting more than 40% of coarse particles to escape the modelled extrathoracic airway through the tracheal outlet. Because the computational domain ends at the tracheal outlet, this fraction represents penetration beyond the upper airway; the subsequent fate of these particles in the tracheobronchial tree and lung is not determined by the present model.

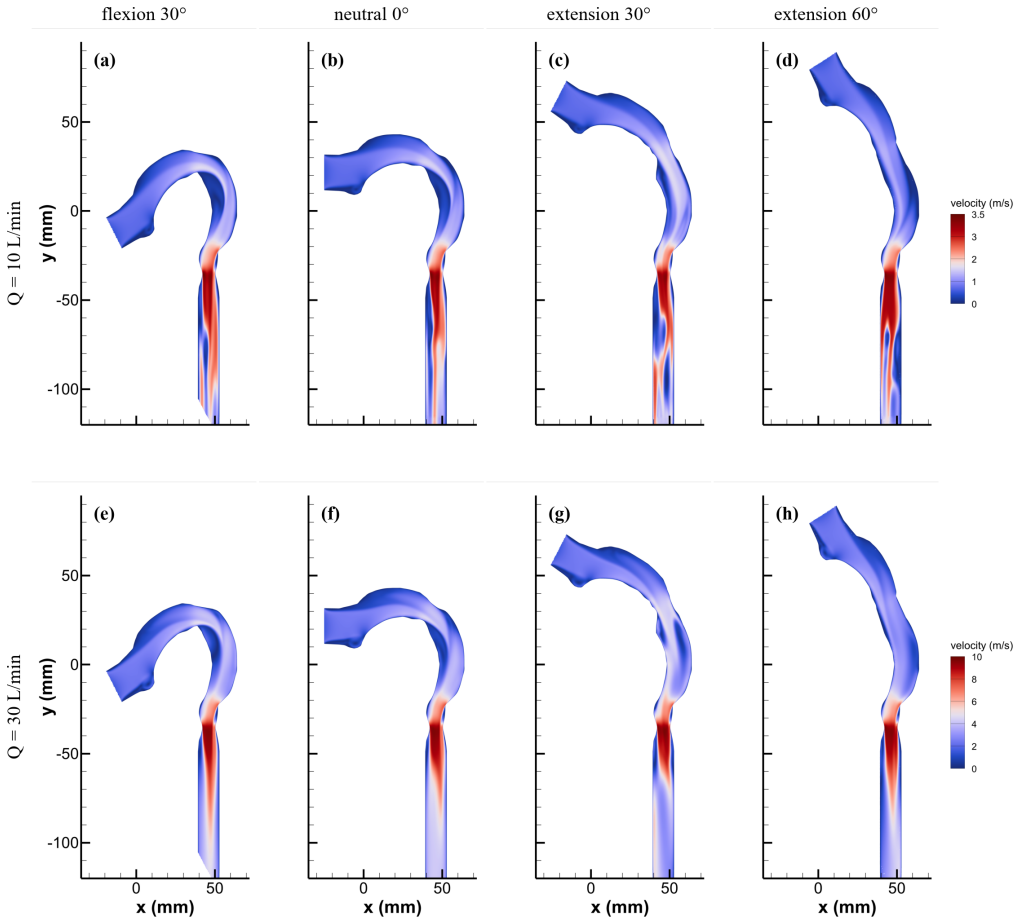


Figure 6. Mid-sagittal speed. (**a**–**d**) Flexion 30°, neutral 0°, extension 30° and extension 60° at 10 L min^{-1}. (**e**–**h**) The same four postures at 30 L min^{-1}. The glottal jet is common to all four postures because the larynx is the same geometry; the postures differ in the oropharynx, where flexion produces a compact core biased to the outer wall and extension a progressively more axial one.

3.3. Targeted Laryngeal Delivery

Targeted deposition within the larynx is detailed in Figure 8d,i and summarised in Table 3. Both the magnitude of peak laryngeal deposition and the optimal particle size were strongly posture-dependent; the comparisons that follow are therefore between the posture-specific maxima, each attained at its own optimal particle size, rather than at a single common size. At 30 L min^{-1}, the highest laryngeal efficiency occurred at 30° extension, depositing 25.7% for d_p = 9 µm. In comparison, peak laryngeal deposition was 15.9% at 11 µm in neutral posture, 10.6% at 13 µm in flexion, and only 5.7% at 29 µm at 60° extension. Comparing these maxima, a moderate head extension of 30° increased the best achievable laryngeal drug capture by a factor of 1.6 relative to neutral posture and 2.4 relative to flexion.

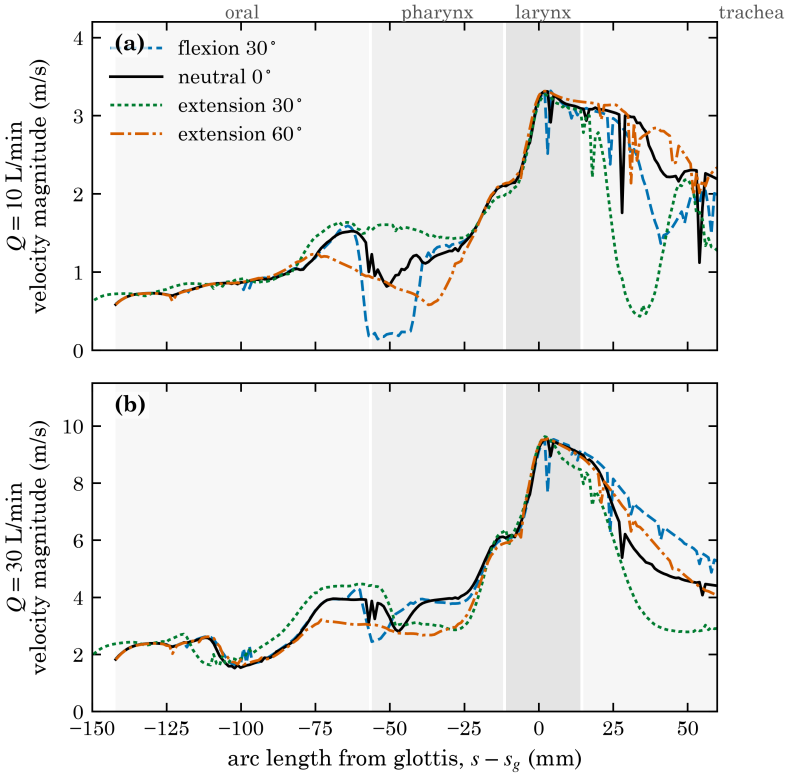


Figure 7. Velocity magnitude on the airway centreline. (**a**) 10 L min^{-1}; (**b**) 30 L min^{-1}.

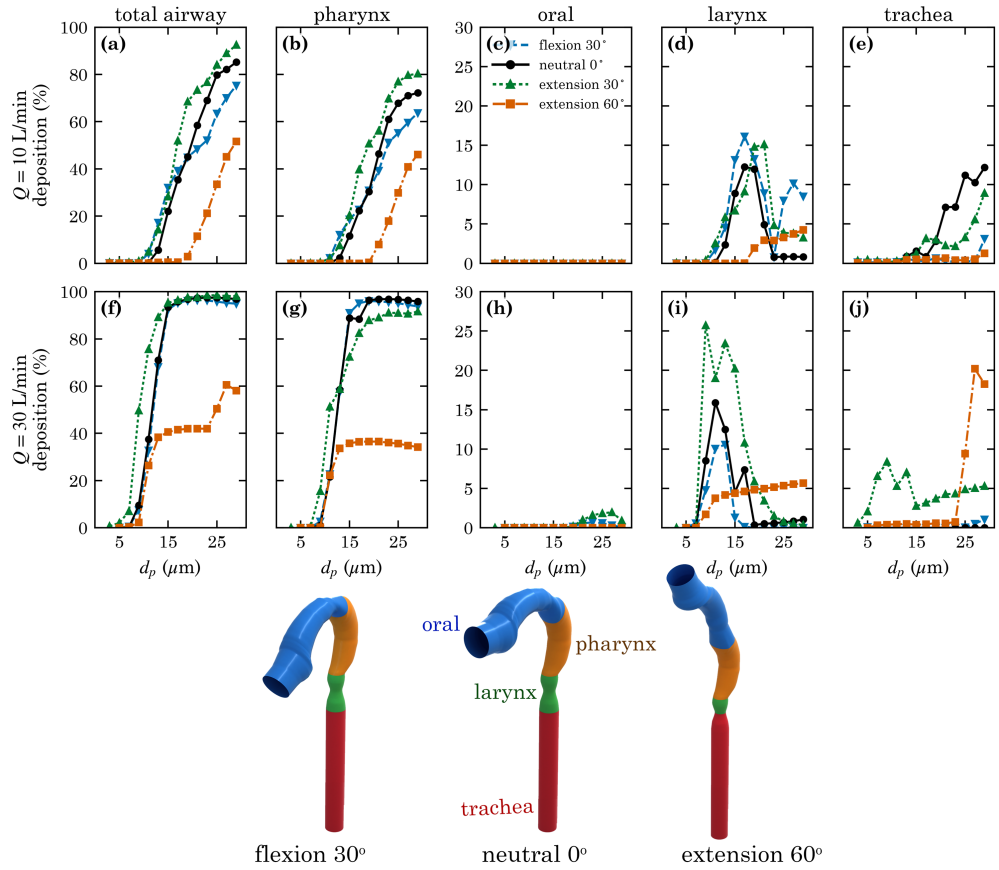


Figure 8. Deposition efficiency against particle diameter, by region. (**a**–**e**) Total airway, pharynx, oral, larynx and trachea at 10 L min^{-1} (top row); (**f**–**j**) the same regions at 30 L min^{-1} (bottom row). There is a change of vertical scale between the first two columns and the last three. Efficiencies are fractions of the inhaled dose.

At 10 L min^{-1}, peak laryngeal deposition shifted toward larger particle sizes: flexion achieved 16.1% at 17 µm, 30° extension reached 15.1% at 21 µm, and neutral 12.2% at 17 µm. These findings demonstrate that head posture and particle aerodynamic size are dependent and that a particle tailored for laryngeal delivery in one posture may be suboptimal in another. Specifically, the 9 µm particle maximises laryngeal deposition at 30° extension but at 30 L min^{-1} deposited less than 1% in the larynx when inhaled passively in the neutral posture at 10 L min^{-1}.

Table 3. Laryngeal targeting. η_{larynx} is the highest laryngeal deposition efficiency over the size range and d_p the size that achieves it; η_{aw} is total airway deposition at d_p and at 29 µm. All efficiencies are fractions of the inhaled dose.

Posture	Q **(L/min)**	η_{larynx} **(%)**	d_p **(µm)**	$\eta_{\mathrm{aw}}(d_p)$ **(%)**	$\eta_{\mathrm{aw}}(29)$ **(%)**
Flexion 30°	10	16.1	17	39.2	75.3
Neutral 0°	10	12.2	17	35.4	85.2
Extension 30°	10	15.1	21	73.4	92.5
Extension 60°	10	4.2	29	51.6	51.6
Flexion 30°	30	10.6	13	68.1	94.9
Neutral 0°	30	15.9	11	37.5	96.9
Extension 30°	30	25.7	9	49.6	98.1
Extension 60°	30	5.7	29	58.1	58.1

3.4. Deposition Distribution Patterns

Deposition distributions along the axial curvature are plotted in Figure 9. At 30 L min^{-1}, the primary deposition location shifted downstream toward the glottis as the bend opened. In flexion, peak deposition was found at $s_{\mathrm{rel}} = -62$ mm in the mid-oropharynx. In neutral posture, the peak shifted downstream to $s_{\mathrm{rel}} = -57$ mm. At 30° extension, the distribution broadened and the peak deposition relocated to $s_{\mathrm{rel}} = -22$ mm, at the laryngeal inlet. At 60° extension, deposition was mainly found in pharynx. In general, the median deposition site appeared to shift from the start of the pharynx toward the larynx as the neck position changed from 30° flexion to 60° extension. However, at 10 L min^{-1}, the deposition location was concentrated to $s_{\mathrm{rel}}(-35, -15)$ mm, with posture influencing deposition quantity rather than its location.

Figure 10 shows deposition sites for 15 µm and 29 µm at both flowrates. For 15 µm at 10 L min^{-1}, deposition occurs on both sides of the pharynx/larynx boundary in flexion, neutral and 30° extension. Therefore, despite Figure 8 recording as deposition across two zones, it is very close to a single area close to the larynx. For 29 µm particles the deposition occurs more frequently upstream of that boundary, at both flow rates. In flexion, neutral and 30° extension, 75–98% deposition occurs and almost all of it lands in the pharynx. The larynx receives very little deposition because very little gets past the pharynx. The 60° extension changes this where deposition shifts further downstream towards the larynx. The overall deposition doesn't change significantly for flexion, neutral and 30° extension but does for 60° extension.

3.5. Deposition Fraction per Size Range

Figure 11 shows the deposition by region, at five diameters. Deposition in the pharynx is most significant in every posture except 60° extension, where the bend is too open to intercept efficiently and much of what is eventually captured is taken up late, by the trachea, at the largest sizes. At 30 L min^{-1} in the neutral posture 96.8% deposition occurs for 21 µm, with larynx and trachea combined never exceeding 4.5%.

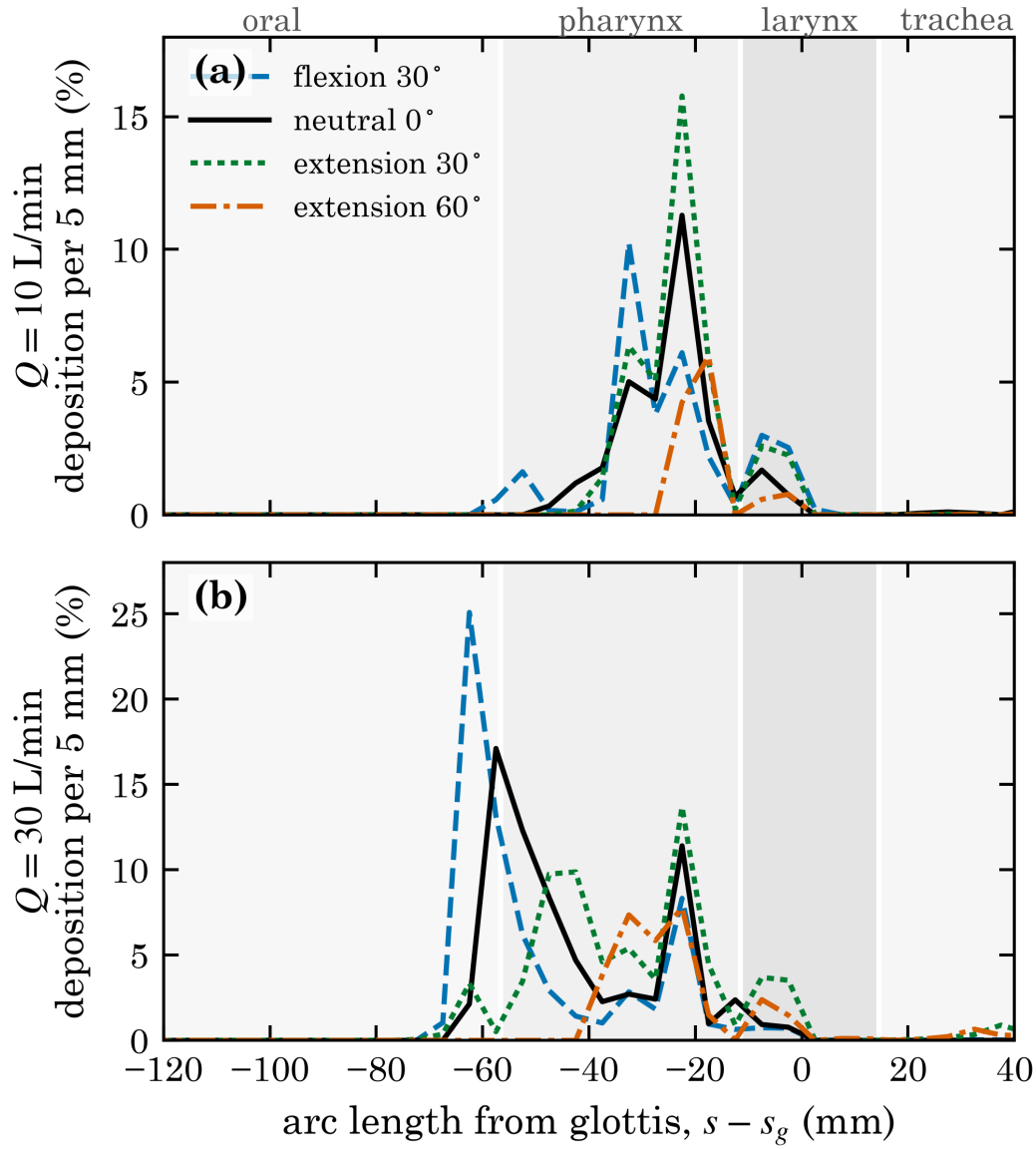


Figure 9. Axial distribution of particle deposition along the airway centreline at (**a**) 10 L min^{-1} and (**b**) 30 L min^{-1} for 30° flexion, neutral posture, and 30° and 60° extension. Deposition is expressed as the percentage of particles deposited per 5 mm interval. Arc length is measured relative to the glottis, $s_{\mathrm{rel}} = s - s_g$; negative values are upstream of the glottis. Shading indicates the airway region: oral, pharynx, larynx and trachea.

For 30° extension, deposition in the larynx peaks (15.1% for 21 µm, 10 L min^{-1} and 25.7% for 9 µm at 30 L min^{-1}). For 60° extension at 30 L min^{-1} the pharyngeal deposition fraction reduces to 35% and a further 18.3% is captured in the trachea only at 29 µm, while the smaller particles exit through the tracheal outlet. The more opened-out bend ($R_c = 84$ mm) no longer presented an effective impaction target.

Targeting the larynx specifically depends on all three parameters: particle diameter, flow rate and geometry. At 30 L min^{-1} and 30° extension, 15 µm particles deposit 20.2% in the larynx; 29 µm particles, at the same flow and posture, deposited only 0.4%, roughly one-fiftieth of the value, from doubling the diameter alone. High total deposition and precise laryngeal targeting are different goals, and even within the same posture, require different particle sizes.

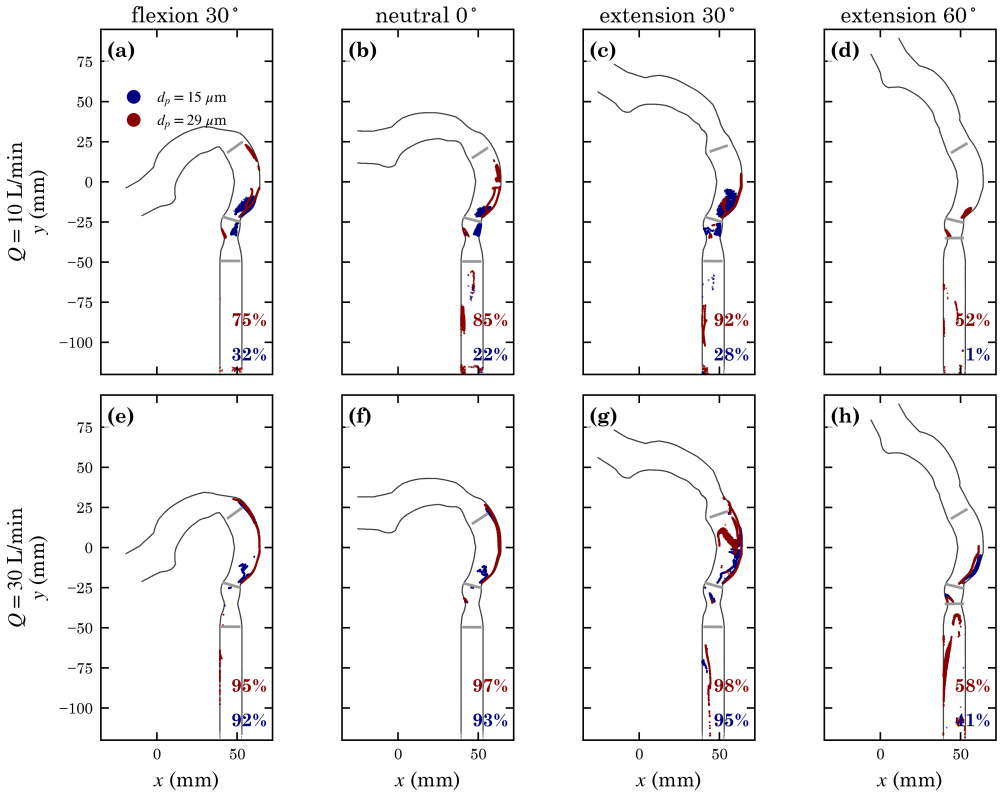


Figure 10. Deposition sites at two representative sizes, overlaid on the mid-sagittal cross-section: 15 µm (navy) and 29 µm (dark red), both shown at both flow rates. (a–d) Flexion 30°, neutral 0°, extension 30° and extension 60° at 10 L min^{-1}. (e–h) The same four postures at 30 L min^{-1}. Grey lines mark boundary of each anatomical region. Deposition values are the total airway deposition at that size.

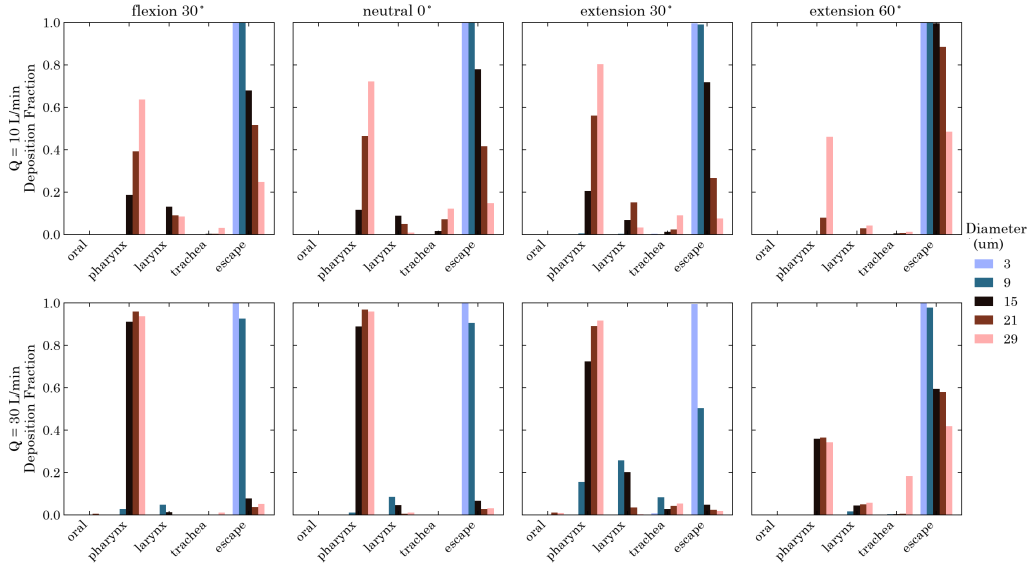


Figure 11. Deposition fraction by region at 3, 9, 15, 21 and 29 µm. Rows are 10 and 30 L min^{-1}; columns are the four postures.

3.6. Head Tilt Influence on Oropharyngeal Bend

Figure 12 combines the geometry and deposition relationships. When plotted against the bend radius R_c, both total airway deposition and laryngeal deposition exhibited an inverted-U profile peaking near $R_c \approx 50$ mm for both flow rates. When plotted against the Dean number De (Figure 12c), the main deposition site collapsed onto a single universal linear relationship across all four postures and both flow rates. A higher Dean number

led to shifting the deposition site further upstream in the pharynx, whereas a lower Dean number allowed the particle to travel further downstream toward the glottis and lower airways. This provides insight into the mechanism of posture-influence particle deposition targeting. For laryngeal deposition, its location and magnitude are determined by two opposing effects:

(i) A tight bend (small R_c, high De) intercepts particles with high efficiency, but does so too far upstream in the oropharynx, reducing the particle amount reaching the larynx.
(ii) An open bend (large R_c, low De) allows particles to pass through the oropharynx, but also reduces its inertial impaction property to capture them at the larynx, causing the particles to pass through towards the lower trachea.

For this passively inhaled set of particles, an optimal intermediate posture exists at approximately 30° extension ($R_c \approx 50$ mm), where the bend is sufficiently sharp to induce impaction, but its physical location has been shifted downstream directly onto the laryngeal inlet.

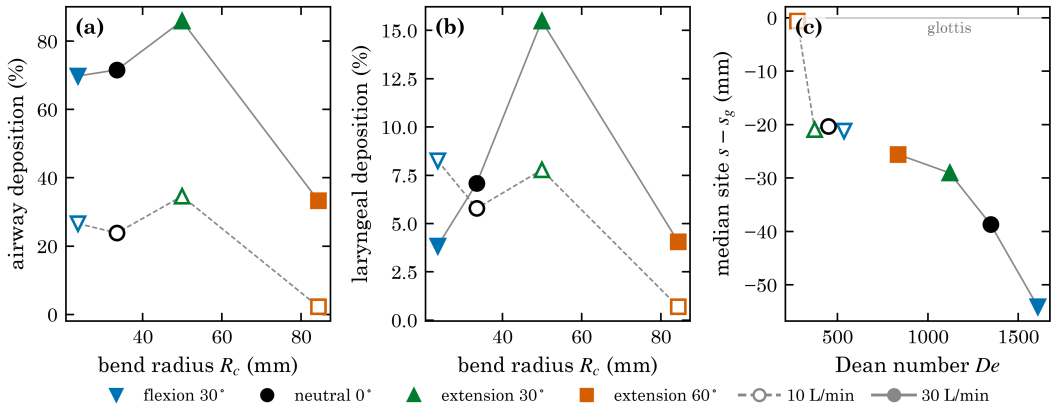


Figure 12. Airway bend as a controlling variable, averaged over 9–21 µm. (**a**) total airway and (**b**) laryngeal deposition against the measured bend radius: both trace an inverted U with a maximum near $R_c \approx 50$ mm at both flow rates. (**c**) local maximum deposition site against Dean number, shows a near-linear relationship across both flow rates and all four postures. Open symbols and dashed lines are 10 L min^{-1}, filled symbols and solid lines 30 L min^{-1}.

3.7. Comparison with Experimental Deposition Correlations

To place the simulations against an external benchmark, total extrathoracic deposition is plotted in Figure 13 against the impaction parameter $d_a^2 Q$, which collapses in vitro and in vivo oral deposition data onto a single curve at fixed geometry [43]. Two reference curves are shown: the correlation fitted by Cheng et al. [11] to measurements in a cast of the human oral airway, $\eta = 1 - \exp(-1.84 \times 10^{-4}\, d_a^2 Q)$, with d_a in µm and Q in L min^{-1}, and the mean in vivo fit compiled by Cheng [43] from volunteer studies (see also the intercomparison of Stahlhofen et al. [44]), $\eta = 1 - \exp(-2.78 \times 10^{-4}\, d_a^2 Q)$. The cast of Cheng et al. [11] is the same oral-airway family from which the present geometry was derived [35], and its particle-size and flow-rate ranges overlap those simulated here, as do those of the tracheobronchial cast of Zhou and Cheng [12].

Deposition of all fourteen particle sizes at both flow rates are shown. Deposition reaches 50% at $d_a^2 Q = 3890$ and 4110 µm^2 L min^{-1} at 10 and 30 L min^{-1}, within 10% of the value of 3770 given by the cast correlation. The simulated results increase with a sharper gradient rise is much steeper where at 30 L min^{-1} deposition increases from 10 to 90% between $d_a^2 Q \approx 2450$ and 6470, compared against the cast correlation. The lower deposition at small $d_a^2 Q$ is expected for a rigid, smooth-walled model with an unconfined mouth inlet and no inhaler- or mouthpiece-induced turbulence, both of which raise extrathoracic

deposition of small particles in vivo [43], and is consistent with the negligible oral-cavity deposition. Flexion follows the neutral posture to within 5 percent at 30 L min^{-1}, but at 10 L min^{-1} its curve is more shallow.

The extended postures depart from the neutral curve in opposite directions. At 30° extension the curve is shifted to smaller impaction parameters. At 60° extension the curve is shifted to larger impaction parameters. At a fixed impaction parameter the four postures differ by up to 66 percentage points at 10 L min^{-1} and 57 at 30 L min^{-1}. Because $d_a^2 Q$ already accounts for particle size and flow rate, these differences reflect the change in airway geometry between postures,due to the curvature of the oropharyngeal bend.

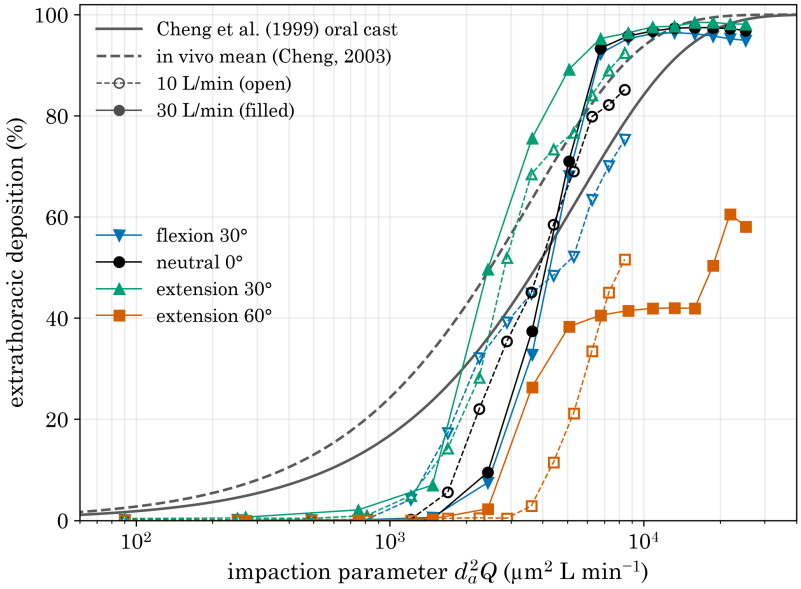


Figure 13. Simulated total extrathoracic deposition against the impaction parameter $d_a^2 Q$ for the four postures and all fourteen particle sizes (open symbols and dashed lines 10 L min^{-1}, filled symbols and solid lines 30 L min^{-1}), compared with the oral-airway cast correlation of Cheng et al. [11] (solid grey) and the mean in vivo fit of Cheng [43] (dashed grey).

4. Discussion

The primary finding of this work is that head posture does not merely adjust particle deposition efficiency; it actively relocates the deposition site along the airway. Because the computational models were constructed to hold the glottic and subglottic anatomy invariant while changing the oral-to-larynx arch, this effect can be attributed principally to the curvature of the oropharyngeal bend rather than confounding inter-subject anatomical variations.

Two secondary geometric differences between the postures nevertheless deserve comment. First, the 30° extension model has a supraglottic centreline 9.1 mm (7%) longer than the other three (Table 1), a consequence of the tangential arc required to blend the rotated oral passage into the fixed larynx (Section 2.1). Because this case also produced the maximum laryngeal deposition, it is reasonable to ask whether the additional path length, rather than the bend radius, is responsible for the downstream displacement of its deposition peak. A length-matched variant was not constructed, since head tilt in vivo changes the length and shape of the supraglottic passage together with its curvature, and a geometry constrained to a fixed path length would not correspond to any posture. Several observations nonetheless indicate that the extra length is not the controlling factor. It is located upstream of the oropharyngeal bend, in the oral cavity and proximal oropharynx, where deposition was negligible (Section 3.2); the bend window and the larynx occupy

the same s_{rel} positions in all four models, so the distance from the end of the bend to the glottis, which sets where a particle crossing streamlines in the bend will strike the wall, is unchanged. The local Stokes number (Equation (1)) depends on the local velocity and diameter, neither of which is altered by a longer upstream run, and the bend Reynolds number of the 30° extension case (Table 2) lies within 2% of the other postures. Most directly, the deposition site of this case falls on the same linear Dean-number relationship as the three length-matched postures (Figure 12c), and the 35 mm downstream shift of its deposition peak relative to the neutral posture is far larger than the 9 mm length difference. Second, the cross-sectional area upstream of the bend differs between postures by up to 41% when compared at equal distance from the glottis; as discussed in Section 3, this largely reflects the comparison of non-corresponding anatomical sections rather than a change in the dimensions of the airway lumen, and the near-constant bend Reynolds numbers confirm that the mean velocity entering the bend was not materially affected.

From a clinical application, adjusting head posture offers a simple, zero-cost, non-invasive patient intervention that can be applied without device redesign. For targeted laryngeal therapies such as local delivery of corticosteroids for chronic laryngitis, vocal fold polyps, or subglottic stenosis, a moderate head extension of 30° combined with higher inhalation flow (30 L min^{-1}) and particle sizing of approximately 9 µm to 11 µm roughly doubles laryngeal deposition relative to a standard neutral posture when particles are inhaled passively. Conversely, over-extending the head to 60° reduces the laryngeal deposition, as the straightened airway allows the particles to pass beyond the modelled extrathoracic airway toward the lower respiratory tract.

For pulmonary drug delivery in therapies for asthma and COPD, oropharyngeal deposition is undesirable, as it wastes medication intended for the lungs [8]. Our results show that opening the oropharyngeal bend via head extension (60°) reduces upper airway deposition from >95% down to ∼40% for large diameter 21 µm to 29 µm particles, allowing more penetration past the glottis and out of the tracheal outlet of the model. Because the computational domain terminates at the trachea, the present results establish only that these particles escape the extrathoracic filter; the proportion that subsequently deposits in the tracheobronchial tree, as opposed to reaching the alveolar region, cannot be determined here and would require coupling to a lower-airway model. With that caveat, head extension may serve as an effective patient instruction to bypass the extrathoracic filter and increase the fraction of the dose available for lung delivery.

The collapse of the data for deposition onto the Dean number indicates that the results may generalise across diverse patient populations. Because $De = Re\sqrt{D/(2R_c)}$ incorporates flow rate, hydraulic diameter, and bend radius, individuals with naturally narrower or sharper pharyngeal passages would be expected to achieve the optimal impaction condition at slightly different tilt angles. Clinical application would benefit from establishing population-wide scaling linking external head angle to internal bend metrics.

5. Limitations

Several limitations should be considered when interpreting these findings:

1. *Solution steady-state assumption.* A steady state simulation was used, with constant inhalation flow rates; a scale-resolving method and a transient breathing profile would enhance these findings to quantify fine-scale vortex shedding and flow-acceleration effects on particle transport.
2. *Transitional turbulence.* Tracheal flow at 30 L min^{-1} corresponds to Re $\approx$ 3200, a transitional regime. The k–ω SST model was used without transitional algebraic corrections or empirical low-Reynolds adjustments.

3. *Geometric construction.* The tangential blending required to re-connect the rotated oral passage to the fixed larynx produced a 9 mm longer supraglottic path for the 30° extension model. This reflects the fact that posture alters path length as well as curvature; the evidence in Section 4 indicates that it did not drive the observed deposition shift, but the bend-radius and path-length effects are not fully separated in this case.
4. *Particle physics, inhaled air and surface compliance.* Particle tracking assumed steady, one-way coupled spherical particles with instantaneous wall trapping. The inhaled air was treated as dry, isothermal and free of pollutants; in reality the temperature and humidity of the inspired air alter the air viscosity entering the Stokes number (by a few percent over the ambient range) and, more importantly for hygroscopic formulations, can increase particle aerodynamic size during transit, shifting deposition upstream. Inhaled particulate pollutants would add to the inert dose considered here but would not change the inertial mechanism. Dynamic factors such as particle cloud dispersion, hygroscopic growth, droplet evaporation, mucosal clearance, and soft-tissue airway compliance during inhalation were not modelled.
5. *Domain extent.* The computational domain ends at the tracheal outlet. Particles reported as escaping the model have penetrated the extrathoracic airway; their subsequent regional deposition in the lower respiratory tract is not resolved.
6. *Cohort scope and experimental validation.* Simulations were conducted on four postures of a simplified airway. While the Dean number scaling provides a theoretical basis for generalisation, and the neutral-posture results agree with published oral-airway cast correlations (Section 3.7), direct experimental validation of the posture effect in anatomical replicas or patient cohorts is needed.

6. Conclusions

A computational investigation of particle transport through four head postures of a single airway model at two inhalation flow rates was conducted using Lagrangian discrete phase tracking. The main conclusions are:

1. Head posture controls extrathoracic particle deposition primarily by altering the curvature of the oropharyngeal bend. Head extension from 30° flexion to 60° extension increased the bend radius R_c from 23.6 mm to 84.3 mm.
2. Total extrathoracic deposition varied with posture, peaking at 30° extension before reducing at 60° extension. Straightening the airway at 60° extension allowed over 40% of coarse particles (21 µm to 29 µm) to bypass extrathoracic impaction and exit the model through the tracheal outlet.
3. The maximum achievable laryngeal drug delivery occurred at 30° extension and 30 L min^{-1}, reaching 25.7% deposition at 9 µm, a 1.6-fold increase over the corresponding maximum for the neutral posture (15.9% at 11 µm) and a 2.4-fold increase over flexion (10.6% at 13 µm). Because each posture attains its maximum at a different particle size, posture and particle aerodynamic diameter must be co-designed to achieve targeted delivery.
4. Across all four postures and both flow rates, the dose-weighted axial deposition site collapsed onto a single relationship with the Dean number, demonstrating that oropharyngeal bend dynamics govern extrathoracic particle partitioning.
5. Plotted against the impaction parameter $d_a^2 Q$, the neutral posture reached 50% extrathoracic deposition within 10% of the value given by the published oral-airway cast correlation, although with a steeper size dependence. At a fixed $d_a^2 Q$, 30° extension raised deposition by up to 40 percent above the neutral posture and 60° extension lowered it by up to 56.

Supplementary Materials: The following supporting information can be downloaded at: https://www.mdpi.com/article/10.3390/fluids11110278/s1. Figure S1. Mesh independence for the 30° flexion airway at 30 L min^{-1}. (a) Velocity magnitude on the mid-sagittal plane for meshes A–D. (b) Velocity difference between successive meshes, with the NMSE of each pair. (c) Velocity difference relative to the finest mesh D, with the NMSE of meshes A–C. Table S1. Meshes used in the mesh-independence study, and the NMSE of the mid-sagittal velocity against the next refined mesh and against the finest mesh (D).

Author Contributions: Conceptualization, K.I.; methodology, X.L., K.I. and B.V.A.; software, X.L. and K.I.; validation, X.L. and K.I.; formal analysis, X.L., K.I. and B.V.A.; investigation, X.L., K.I. and B.V.A.; resources, K.I.; data curation, X.L., K.I. and B.V.A.; writing—original draft preparation, X.L., K.I. and B.V.A.; writing—review and editing, X.L., K.I. and B.V.A.; visualization, X.L., K.I. and B.V.A.; supervision, K.I.; project administration, K.I.; funding acquisition, K.I.. All authors have read and agreed to the published version of the manuscript.

Funding: This research received no external funding.

Institutional Review Board Statement: Not applicable.

Informed Consent Statement: Not applicable.

Data Availability Statement: The raw data supporting the conclusions of this article will be made available by the authors on request.

Acknowledgments: This research was undertaken with the assistance of resources from the National Computational Infrastructure (NCI Australia), an NCRIS enabled capability supported by the Australian Government.

Conflicts of Interest: The authors declare no conflicts of interest.

References

1. Longest, P.W.; Bass, K.; Dutta, R.; Rani, V.; Thomas, M.L.; El-Achwah, A.; Hindle, M. Use of computational fluid dynamics deposition modeling in respiratory drug delivery. *Expert Opin. Drug Deliv.* **2019**, *16*, 7–26. [CrossRef]
2. Kleinstreuer, C.; Shi, H.; Zhang, Z. Computational analyses of a pressurized metered dose inhaler and a new drug–aerosol targeting methodology. *J. Aerosol Med.* **2007**, *20*, 294–309. [CrossRef]
3. Faizal, W.; Ghazali, N.N.N.; Khor, C.; Badruddin, I.A.; Zainon, M.Z.; Yazid, A.A.; Ibrahim, N.B.; Razi, R.M. Computational fluid dynamics modelling of human upper airway: A review. *Comput. Methods Programs Biomed.* **2020**, *196*, 105627. [CrossRef]
4. Cotton, R.T. Management of subglottic stenosis. *Otolaryngol. Clin. N. Am.* **2000**, *33*, 111–130. [CrossRef]
5. Hull, J.H.; Backer, V.; Gibson, P.G.; Fowler, S.J. Laryngeal dysfunction: Assessment and management for the clinician. *Am. J. Respir. Crit. Care Med.* **2016**, *194*, 1062–1072. [CrossRef]
6. Chmielewska, M.; Akst, L.M. Dysphonia associated with the use of inhaled corticosteroids. *Curr. Opin. Otolaryngol. Head Neck Surg.* **2015**, *23*, 255–259. [CrossRef]
7. Xi, J.; Xi, J.; Zhao, W.; Zhang, Y. Targeted delivery of therapeutic aerosols to the oral cavity and pharynx. *J. Aerosol Med. Pulm. Drug Deliv.* **2016**, *29*, 342–354.
8. Roland, N.J.; Bhalla, R.K.; Earis, J. The local side effects of inhaled corticosteroids. *Chest* **2004**, *126*, 213–219. [CrossRef]
9. Vahaji, S.; Nguyen, N.H.; Shang, Y.; Inthavong, K. Sedimentation effects on particle position and inertial deposition in 90° circular bends. *Powder Technol.* **2021**, *393*, 722–733. [CrossRef]
10. Chan, T.L.; Lippmann, M. Experimental measurements and empirical modelling of the regional deposition of inhaled particles in humans. *Am. Ind. Hyg. Assoc. J.* **1980**, *41*, 399–409. [CrossRef]
11. Cheng, Y.S.; Zhou, Y.; Chen, B.T. Particle deposition in a cast of human oral airways. *Aerosol Sci. Technol.* **1999**, *31*, 286–300. [CrossRef]
12. Zhou, Y.; Cheng, Y.S. Particle deposition in a cast of human tracheobronchial airways. *Aerosol Sci. Technol.* **2005**, *39*, 492–500. [CrossRef]
13. Nordlund, M.; Belka, M.; Kuczaj, A.K.; Lizal, F.; Jedelsky, J.; Elcner, J.; Jicha, M.; Sauser, Y.; Le Bouhellec, S.; Cosandey, S.; et al. Multicomponent aerosol particle deposition in a realistic cast of the human upper respiratory tract. *Inhal. Toxicol.* **2017**, *29*, 113–125. [CrossRef]
14. Lennon, S.; Zhang, Z.; Lessmann, R.; Webster, S. Experiments on particle deposition in the human upper respiratory system. *Aerosol Sci. Technol.* **1998**, *28*, 464–474. [CrossRef]

15. Darquenne, C. Aerosol Deposition in Health and Disease. *J. Aerosol Med. Pulm. Drug Deliv.* **2012**, *25*, 140–147. [CrossRef]
16. Cheng, Y.S. Mechanisms of Pharmaceutical Aerosol Deposition in the Respiratory Tract. *AAPS PharmSciTech* **2014**, *15*, 630–640. [CrossRef]
17. Wang, Y.; Elghobashi, S. On locating the obstruction in the upper airway via numerical simulation. *Respir. Physiol. Neurobiol.* **2014**, *193*, 1–10. [CrossRef]
18. Tsuda, A.; Henry, F.S.; Butler, J.P. Particle Transport and Deposition: Basic Physics of Particle Kinetics. *Compr. Physiol.* **2013**, *3*, 1437–1471. [CrossRef]
19. Berger, S.A.; Talbot, L.; Yao, L.S. Flow in Curved Pipes. *Annu. Rev. Fluid Mech.* **1983**, *15*, 461–512. [CrossRef]
20. Frederix, E.M.A.; Kuczaj, A.K.; Nordlund, M.; Veldman, A.E.P.; Geurts, B.J. Eulerian modeling of inertial and diffusional aerosol deposition in bent pipes. *Comput. Fluids* **2017**, *159*, 217–231. [CrossRef]
21. Inthavong, K. A unifying correlation for laminar particle deposition in 90-degree pipe bends. *Powder Technol.* **2019**, *345*, 99–110. [CrossRef]
22. Gampp Lehmann, K.; Sticher, H. Posture and function: What helps us swallow. In *Facial-Oral Tract Therapy (FOTT) for Eating, Swallowing, Nonverbal Communication and Speech*; Springer: Berlin/Heidelberg, Germany, 2021; pp. 45–72.
23. Ardran, G.; Kemp, F. The Mechanism of the Larynx—II The epiglottis and closure of the larynx. *Br. J. Radiol.* **1967**, *40*, 372–389. [CrossRef]
24. Traser, L.; Burdumy, M.; Richter, B.; Vicari, M.; Echternach, M. The effect of supine and upright position on vocal tract configurations during singing—A comparative study in professional tenors. *J. Voice* **2013**, *27*, 141–148. [CrossRef]
25. Zafar, H.; Albarrati, A.; Alghadir, A.H.; Iqbal, Z.A. Effect of different head-neck postures on the respiratory function in healthy males. *BioMed Res. Int.* **2018**, *2018*, 4518269. [CrossRef]
26. Appel, M.; Childs, A.; Healey, E.; Markowitz, S.; Wong, S.; Mead, J. Effect of posture on vital capacity. *J. Appl. Physiol.* **1986**, *61*, 1882–1884. [CrossRef]
27. Taherian, S.; Rahai, H.; Gomez, B.Z.; Waddington, T.; Bonifacio, J.R. Tracheal stenosis: A CFD approach for evaluation of drug delivery. In *Proceedings of the ASME International Mechanical Engineering Congress and Exposition*; American Society of Mechanical Engineers: New York, NY, USA, 2015; Volume 57380, p. V003T03A096.
28. Xi, J.; Yuan, J.E.; Yang, M.; Si, X.; Zhou, Y.; Cheng, Y.S. Parametric study on mouth–throat geometrical factors on deposition of orally inhaled aerosols. *J. Aerosol Sci.* **2016**, *99*, 94–106. [CrossRef]
29. Feng, Y.; Zhao, J.; Kleinstreuer, C.; Wang, Q.; Wang, J.; Wu, D.H.; Lin, J. An in silico inter-subject variability study of extra-thoracic morphology effects on inhaled particle transport and deposition. *J. Aerosol Sci.* **2018**, *123*, 185–207. [CrossRef]
30. Xi, J.; Yang, T. Variability in oropharyngeal airflow and aerosol deposition due to changing tongue positions. *J. Drug Deliv. Sci. Technol.* **2019**, *49*, 674–682. [CrossRef]
31. Bannister, A.K.; Macbeth, R.G. Direct laryngoscopy and the alignment of the airway axes. *Lancet* **1944**, *244*, 651–654. [CrossRef]
32. Adnet, F.; Borron, S.W.; Lapostolle, F.; Lapandry, X. Study of the "sniffing position" by magnetic resonance imaging. *Anesthesiology* **2001**, *94*, 83–86. [CrossRef]
33. Adnet, F.; Baillard, C.; Nicolas-Robin, A.; Heym, L.; Revély, J.P.; Gilles, B.; Cupa, M. Randomized study comparing the "sniffing position" with simple head extension for laryngoscopic views in elective surgery patients. *Anesthesiology* **2001**, *95*, 836–841. [CrossRef]
34. Vara Almirall, B.; Wong, C.Y.J.; Pille, P.; Ang, H.Q.; Traini, D.; Singh, N.; Inthavong, K. In vitro inhalation and deposition of salbutamol in upper airway geometries. *Pharm. Res.* **2026**, *43*, 453–463. [CrossRef]
35. Cheng, K.H.; Cheng, Y.S.; Yeh, H.C.; Swift, D.L. Measurements of airway dimensions and calculation of mass transfer characteristics of the human oral passage. *J. Biomech. Eng.* **1997**, *119*, 476–482. [CrossRef]
36. Zhang, Z.; Kleinstreuer, C. Airflow structures and nano-particle deposition in a human upper airway model. *J. Comput. Phys.* **2004**, *198*, 178–210. [CrossRef]
37. Yousefi, M.; Inthavong, K.; Tu, J. Effect of pressurized metered dose inhaler spray characteristics and particle size distribution on drug delivery efficiency. *J. Aerosol Med. Pulm. Drug Deliv.* **2017**, *30*, 359–372. [CrossRef]
38. Kleinstreuer, C.; Zhang, Z.; Li, Z. Modeling airflow and particle transport/deposition in pulmonary airways. *Respir. Physiol. Neurobiol.* **2008**, *163*, 128–138. [CrossRef]
39. Zhang, Z.; Kleinstreuer, C.; Donohue, J.F.; Kim, C. Comparison of micro-and nano-size particle depositions in a human upper airway model. *J. Aerosol Sci.* **2005**, *36*, 211–233. [CrossRef]
40. Inthavong, K.; Chetty, A.; Shang, Y.; Tu, J. Examining mesh independence for flow dynamics in the human nasal cavity. *Comput. Biol. Med.* **2018**, *102*, 40–50. [CrossRef]
41. Frank-Ito, D.O.; Wofford, M.; Schroeter, J.D.; Kimbell, J.S. Influence of Mesh Density on Airflow and Particle Deposition in Sinonasal Airway Modeling. *J. Aerosol Med. Pulm. Drug Deliv.* **2016**, *29*, 46–56. [CrossRef]
42. Menter, F.R. Two-equation eddy-viscosity turbulence models for engineering applications. *AIAA J.* **1994**, *32*, 1598–1605. [CrossRef]

43. Cheng, Y.S. Aerosol deposition in the extrathoracic region. *Aerosol Sci. Technol.* **2003**, *37*, 659–671. [CrossRef]
44. Stahlhofen, W.; Rudolf, G.; James, A.C. Intercomparison of experimental regional aerosol deposition data. *J. Aerosol Med.* **1989**, *2*, 285–308. [CrossRef]

Disclaimer/Publisher's Note: The statements, opinions and data contained in all publications are solely those of the individual author(s) and contributor(s) and not of MDPI and/or the editor(s). MDPI and/or the editor(s) disclaim responsibility for any injury to people or property resulting from any ideas, methods, instructions or products referred to in the content.